Direct measurement of the viscoelectric effect in water

Di Jin[a,1], Yongyun Hwang[b], Liraz Chai[c], Nir Kampf[a], and Jacob Klein[a,1]

[a]Department of Molecular Chemistry and Materials Science, Weizmann Institute of Science, Rehovot 76100, Israel; [b]Department of Aeronautics, Imperial College, London SW7 2BX, United Kingdom; and [c]Institute of Chemistry, The Hebrew University of Jerusalem, Jerusalem 91904, Israel

Edited by Matthew Tirrell, Pritzker School of Molecular Engineering, The University of Chicago, Chicago, IL; received July 25, 2021; accepted November 12, 2021

The viscoelectric effect concerns the increase in viscosity of a polar liquid in an electric field due to its interaction with the dipolar molecules and was first determined for polar organic liquids more than 80 y ago. For the case of water, however, the most common polar liquid, direct measurement of the viscoelectric effect is challenging and has not to date been carried out, despite its importance in a wide range of electrokinetic and flow effects. In consequence, estimates of its magnitude for water vary by more than three orders of magnitude. Here, we measure the viscoelectric effect in water directly using a surface force balance by measuring the dynamic approach of two molecularly smooth surfaces with a controlled, uniform electric field between them across highly purified water. As the water is squeezed out of the gap between the approaching surfaces, viscous damping dominates the approach dynamics; this is modulated by the viscoelectric effect under the uniform transverse electric field across the water, enabling its magnitude to be directly determined as a function of the field. We measured a value for this magnitude, which differs by one and by two orders of magnitude, respectively, from its highest and lowest previously estimated values.

viscoelectric effect | electrokinetic phenomena | viscosity/electric field coupling | surface forces balance

The viscoelectric effect concerns the change in the viscosity of polar liquids in the presence of an electric field (1–3). It arises from the interaction of the field with the dipolar molecules, and while its molecular origins are still not well understood (4–6), it has considerable relevance in areas ranging from surface potential measurements (7–9) and boundary lubrication (10) to nanofluidics and its applications (11–13). Knowing the magnitude of the viscoelectric effect is thus of clear importance. It was first measured by Andrade and Dodd (1–3) for a range of polar organic liquids, by monitoring their flow in a narrow channel between metal electrodes across which a known electric field $\boldsymbol{E}$ was applied, and quantified via a viscoelectric coefficient f using an empirical relation based on their results:

$$\eta(\boldsymbol{E}) = \eta_0(1 + f|\boldsymbol{E}|^2), \quad [1]$$

a simplified analysis leading to such a relation is given in Ref. (8). Here, η_0 is the unperturbed bulk liquid viscosity (i.e., in the absence of any field). For the case of water, however, the most ubiquitous and important polar liquid, measurement of its viscosity in the presence of a strong, uniform field presents a strong challenge (as discussed later in this section), and to our knowledge no such direct measurements have been reported. Over the past six decades, therefore, the magnitude of the viscoelectric effect in water has been only indirectly estimated by extrapolation from its values for organic liquids (8), from estimates of its effect on electrokinetic phenomena (11, 14–19), or by other approaches (7, 12, 20, 21). These estimated values, as expressed in the viscoelectric coefficient f, vary over more than three orders of magnitude, ranging from $f \sim 10^{-17}$–2.5×10^{-14} $(\mathrm{V/m})^2$ (*SI Appendix*, Section 7). For completeness, we note that results contradictory to the viscoelectric model have also been reported (22) (i.e., suggesting a decreased water viscosity in an electric field). The reasons for the large span of these estimated f values were attributed to various factors such as solid/liquid coupling, varying ionic sizes, and varying water permittivity (12, 19); however, while these factors may play some role, there is no evidence that they could lead to such large discrepancies.

We believe, rather, that the origin of the large variance in the estimated magnitude of the viscoelectric effect arises because none of the experimental studies on water to date in which the f values were estimated was direct, in the sense of probing how the water viscosity varied with field in a uniform electric field. In all cases, viscosity changes were assumed to occur only in the nonuniform, rapidly decaying electrostatic potential near charged surfaces immersed in water. Changes in electrophoretic mobility, electro-osmosis, or hydrodynamic dissipation or water mobility between similarly charged solid surfaces were then attributed to some mean viscosity increase in these thin surface-adjacent layers (7, 11, 12, 14–21). In practice, however, the effect on these electrokinetic phenomena of viscosity or water mobility changes in the thin layers where such nonuniform, rapidly decaying fields are present is not easy to quantify reliably, especially in the presence of salt ions (12). At the same time, measuring the viscosity of water in a uniform electric field between two surfaces at different potentials, as was done for the polar organic solvents (2, 3) and which would provide a direct determination of its viscoelectric effect, presents a considerable difficulty. This is due to two main factors and arises because, in contrast to organic solvents, water may self-dissociate. Firstly, the potential difference that

Significance

The viscosity of polar liquids increases in an electric field because of its interaction with the dipolar molecules. This viscoelectric effect was measured for organic liquids, but for water, the most important polar liquid, where it is crucial in areas from surface potential determination to nanofluidic applications, this is very challenging, and no direct measurements have been carried out to date. Consequently, estimates of its magnitude in water vary by more than a thousandfold. Here, we use a surface force balance to measure the dynamic approach of two molecularly smooth surfaces with a uniform, controlled electric field between them across water; this is modulated by the water viscosity and hence the viscoelectric effect, enabling its magnitude to be directly determined.

Author contributions: D.J., L.C., and J.K. designed research; D.J. and N.K. performed research; D.J. and Y.H. analyzed data; and D.J. and J.K. wrote the paper.

The authors declare no competing interest.

This article is a PNAS Direct Submission.

This article is distributed under Creative Commons Attribution-NonCommercial-NoDerivatives License 4.0 (CC BY-NC-ND).

[1]To whom correspondence may be addressed. Email: di.jin@weizmann.ac.il or jacob.klein@weizmann.ac.il.

This article contains supporting information online at http://www.pnas.org/lookup/suppl/doi:10.1073/pnas.2113690119/-/DCSupplemental.

Published December 30, 2021.

Downloaded from https://www.pnas.org by Imperial College London Library on August 25, 2022 from IP address 155.198.10.231.

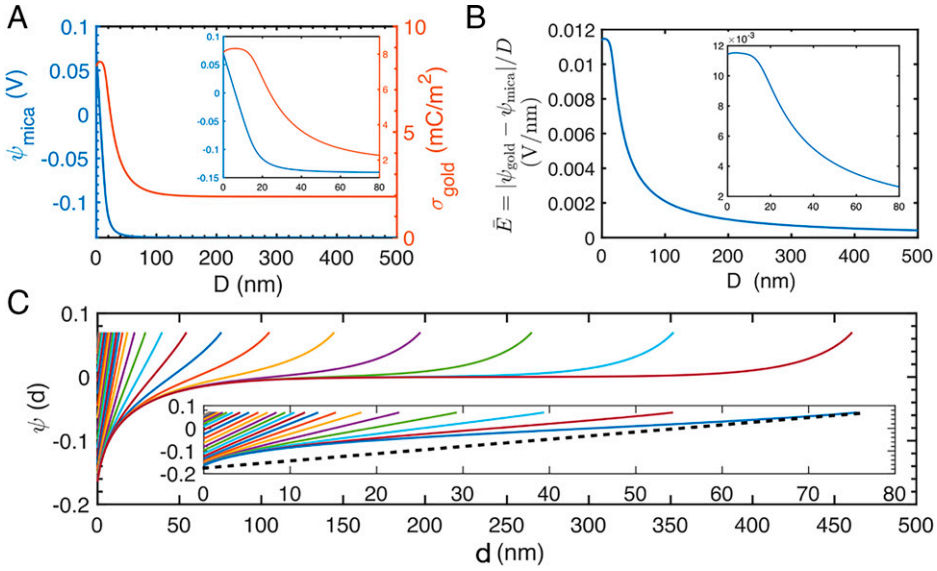

Fig. 1. Numerical solution to the nonlinearized PB equation with $\sigma_{mica} = -8.1$ mC/m^2, $\psi_{gold} = 0.07$ V, and ion concentration $c_b = 8 \times 10^{-5}$ M, corresponding to the conditions of Fig. 4*A*. (*A*) Surface potential on the mica surface and surface charge on the gold surface as a function of separation *D*. (*B*) Average electric field approximated as ($|\psi_{gold} - \psi_{mica}|/D$). (*C*) Local potential ψ as a function of distance *d* from the mica surface for different separations *D*. Dashed line in larger-scale inset is an eye guide of a linear approximation.

may be applied between the surfaces across water is limited, if electrolysis is to be avoided (23, 24), and secondly, electrostatic screening implies that the field decays strongly (within a Debye screening length) away from the surfaces (25–27). Even in purified water with no added salt (as in the present study), the potential decays rapidly away from a charged surface (see, e.g., Fig. 1*C*), so that to measure viscosity in a uniform field between two surfaces, one would require flow channels of width of order some tens of nanometers or less, presenting a major challenge.

In the present study, we overcome this by directly probing the viscosity of purified water across which a uniform electric field acts while it is confined between two surfaces in a surface force balance (SFB). In our experiments, a molecularly smooth gold surface at a controlled (positive) surface potential approaches an atomically smooth mica surface at constant surface (negative) charge density, so that a known electric field acts across the water-filled gap of width *D* between them; moreover, this field is very close to uniform at the most relevant surface separations ($D \lesssim 30$ nm, Fig. 1*C*). The dynamics of approach is strongly modulated by the viscous damping due to squeeze-out of the water as *D* decreases, and hence by its viscosity in the uniform electric field; by monitoring the approach rate of the surfaces at high temporal (millisecond) and spatial (approximately angstrom) resolutions, we are able therefore to directly evaluate the magnitude of the viscoelectric effect (the value of *f*).

Results and Discussion

Electric Field Between Interacting Surfaces across Water. The SFB has been traditionally used to measure interactions between two single-crystal, atomically smooth mica surfaces as a function of their separation *D*, where, in water, each mica surface is negatively charged because of the dissociation of potassium ions (25, 26, 28), corresponding to a constant-charge surface with charge density σ_{mica}. Detailed descriptions of the SFB appear elsewhere (28, 29). More recently, by replacing one of the mica sheets with a template-stripped, molecularly smooth gold surface (30) (rms roughness ~2 Å, *SI Appendix*, Section 6; Fig. 2*A*) and controlling the potential ψ_{gold} of the gold with a potentiostat in a three-electrode configuration (31, 32) (Fig. 2*C*), it is possible to measure interactions between the surfaces at different potentials and thus with an electric field acting between them (32).

Purified water with no added salt (*Materials and Methods*) was added to the SFB bath immersing the mica and gold surfaces. When a positive potential is applied to the gold, a long-ranged electrostatic attraction acts between the surfaces, as previously observed (28, 32). The dynamics of approach was initiated (at time $t = 0$, at a separation $D = D_0 > 300$ nm, larger than the range of any surface interactions) by imposing a steady extension on the piezo crystal, on which the top (gold) surface is mounted, at a speed $v_{app} < 10$ nm/s. This drives the gold surface toward the lower mica surface, which is mounted on a spring of constant *k*. Onset of the long-range electrostatic attraction is observed at surface separations *D* ~100 nm, and at lower *D* values, the surfaces jump into contact because of an Euler-like spring-instability (33). During the approach, the separation $D(t)$ is obtained from the interference fringes of equal chromatic order (FECO, Fig. 2*B*), using fast video recording (~10^3 fps) at millisecond intervals. The typical noise in $D(t)$ is ~2 Å. The interaction between the surfaces as they approach arises from both conservative forces, i.e., electrostatic forces F_{PB} described by the Poisson-Boltzmann (PB) equation and van der Waals (vdW) forces between the gold and mica surfaces across water, F_{vdW}, together with hydrodynamic forces due to the finite approach speed of the surfaces. The relative motion of the surfaces during the approach obeys the following equation, as previously described (33):

$$F_{tot}(D) = m\left(\frac{d^2D}{dt^2}\right) - k(D_0 - D(t) + v_{app}t) + 6\pi R^2\eta\left[\left(\frac{dD}{dt}\right)/D(t)\right] \quad [2]$$

The term on the left is the total conservative surface force $F_{tot} = F_{vdW} + F_{PB}$ (*SI Appendix*, section 1), which is balanced by the inertial term (first term on right), the force due to distortion of the spring from its unperturbed state at separation D_0 at $t = 0$ (second term on right), and the hydrodynamic resistance (third term on right), where *R* is the mean radius of curvature of the curved mica and gold surfaces and η is the water viscosity in the gap, which depends on the electric field through the viscoelectric effect (Eq. **1**). The inertial term (where *m* ~2 gm is the mass of the lower lens) is readily shown to be negligible compared to the other terms (33). In this study, the electroviscous effect (34–37),

Downloaded from https://www.pnas.org by Imperial College London Library on August 25, 2022 from IP address 155.198.10.231.

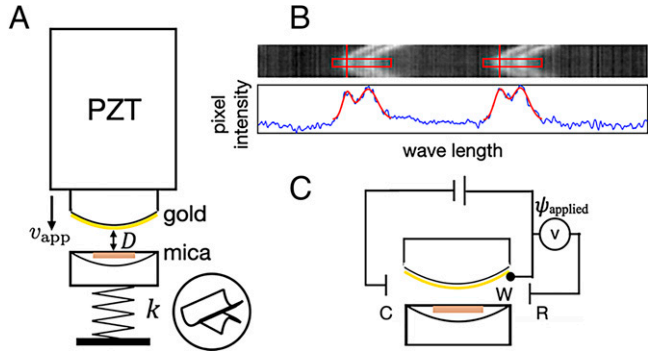

Fig. 2. Schematics of the SFB setup (29) (*Materials and Methods*). (*A*) Schematic of the smooth gold surface coating a cylindrical lens, mounted on the piezoelectric tube (PZT), facing the back-silvered mica surface glued on a similar lens, in a crossed-cylinder configuration, supported by the spring *k*. (*B*) Images of FECO formed by white light interference between the gold and the silver layers were recorded at high frame rates (up to 1,000 fps) during the approach of the surfaces. Separation (*D*) was evaluated with subnanometer precision from the wavelengths of the fringe tips obtained from a double Gaussian fit to the pixel intensity profile (FECO image shown here taken at 100 fps for better contrast). (*C*) An electric potential (controlled by a potentiostat) is applied to the gold surface via a three-electrode configuration. The counter (C) and reference (R) electrodes were constructed with platinum wires. The working (W) electrode is the gold surface. $\psi_{applied}$ is imposed by the potentiostat.

which describes the resistance to the flow of the counterions in the diffuse double layers adjacent to the gold and mica surfaces (and should not be confused with the viscoelectric effect, which is the subject of our study), is negligible because of the low ion concentration and may therefore be safely ignored in the hydrodynamic resistance term (*SI Appendix*, Section 4). The electric field in the gap $E(D)$ can be evaluated by the PB equation for given ψ_{gold} and σ_{mica}. ψ_{gold} is unknown a priori from the applied potential on the gold because of the usage of a pseudoelectrode (Fig. 2*C*) but may be evaluated from the force versus distance profile $F(D)$ as the surfaces approach (32); σ_{mica} is controlled by the equilibrium of surface cation adsorption, mostly dependent on the proton concentration in the immediate vicinity of the surface (26), and may likewise be determined from the $F(D)$ profile (32).

Typical force versus separation approach profiles are shown in Fig. 3 *A* and *B* (normalized as F_{tot}/R in the Derjaguin approximation), evaluated from the experimentally measured $D(t)$ via Eq. **2** on the assumption that the viscosity is at its unperturbed (i.e., zero field) bulk water value η_0 throughout. This is a good approximation at separations $D > 40$ nm, where the mean electric field between the mica and gold surfaces is so low (see Fig. 1*B*) that differences between η and η_0 are negligible at all $D >$ 40 nm. This allows the unknown parameters σ_{mica}, ψ_{gold}, and bulk concentration c_b to be extracted through comparison with solutions of the PB equation (together with vdW forces) for $D > 40$ nm (details in *Materials and Methods* and *SI Appendix*, Section 1). The resulting theoretical fits are shown in Fig. 3 *A* and *B*; the deviation at $D < \sim$30 nm between the experimental curve deduced from Eq. **2** and the theoretical force fit based on the PB and vdW equations is due entirely to the fact that the viscoelectric effect is not taken into account in Eq. **2**, as confirmed in the next section. Inset in Fig. 3*B* is shown for comparison data from an earlier study (32) of interactions between mica and gold at the same applied potentials on the gold (0.2 V), in which σ_{mica}, ψ_{gold}, and bulk concentration c_b were independently determined and were evaluated from Eq. **2** ignoring the viscoelectric effect. These data show, as expected, close similarity to the present study at $D > \sim$40 nm (the slight differences at lower D values are likely due to the much lower video acquisition rate and thus the time resolution in the earlier work).

Using these parameters obtained from the force profiles in Fig. 3, we may evaluate the potential on the mica surface ψ_{mica}, the charge density on the gold surface σ_{gold}, and the potential in the gap $\psi(d)$ $(0 < d < D)$ by numerically solving the nonlinearized PB equation (*SI Appendix*, Section 1) at varying separations D, as shown in Fig. 1.

Fig. 1*A* shows that as the separation D decreases, σ_{gold} approaches $-\sigma_{mica}$ and ψ_{mica} approaches ψ_{gold}, as earlier discussed (28). Ultimately the two surfaces mutually neutralize when in contact. The mean electric field $\bar{E} = |\psi_{gold} - \psi_{mica}|/D$ is shown in Fig. 1*B*. Although ψ_{mica} becomes less negative as D decreases, $\bar{E}$ increases because of the hyperbolically increasing factor $1/D$ and eventually plateaus as D approaches zero. For our analysis with the viscoelectric model (Eq. **1**), $E = \bar{E}$ is an excellent approximation at small separations as $\psi(d)$ becomes more linear in trend (Fig. 1*C*) so that the field is essentially uniform for $D < \sim$40 nm. At large separations, our fits to Eq. **2** are seen to be justified by the small magnitude of $\bar{E}$; at an order of 0.004 V/nm or less, water viscosity is enhanced by ~1.6% or less, assuming a viscoelectric coefficient of order 10^{-15} m^2/V^2 (see next section), which, as noted earlier, has negligible impact on the approach dynamics at $D > 40$ nm.

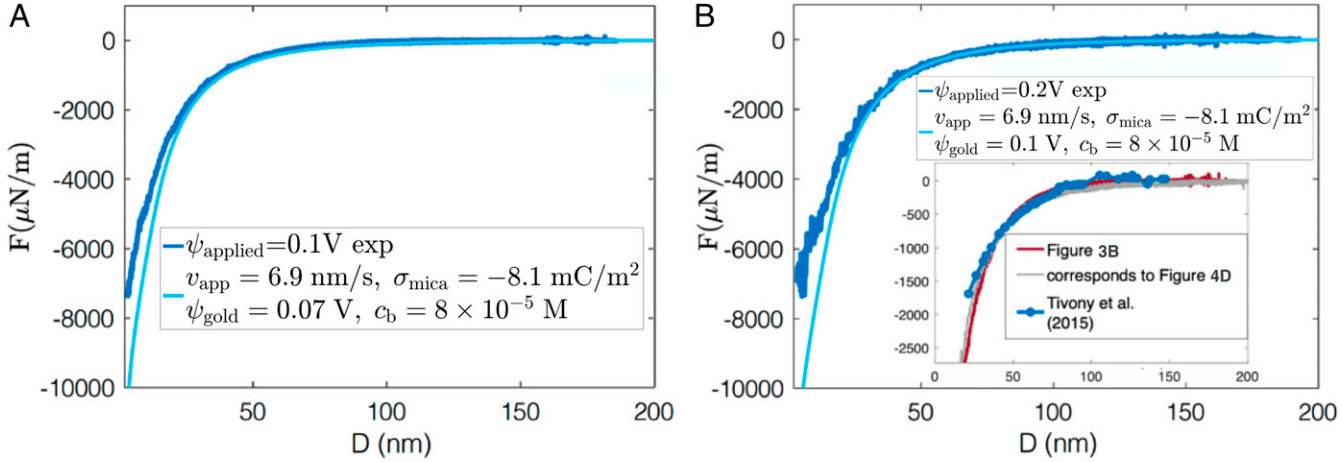

Fig. 3. (*A*, *B*) Representative force versus surface separation profiles evaluated from the experimentally measured $D(t)$ variation via Eq. **2**, assuming unperturbed viscosity of water. The smooth curve is the predicted $F_{BP} + F_{vdW}$ fitted to the region $D > \sim$40 nm and used to extract values of σ_{mica}, c_b, and ψ_{gold} (see *SI Appendix* for details). The inset in *B* compares typical force profiles in our study (gray and red curves) with results from an earlier study by Tivony et al. (32) (blue dots) between mica and gold surfaces at the same applied gold potential (0.2 V), showing close correspondence for $D > \sim$40 nm.

Downloaded from https://www.pnas.org by Imperial College London Library on August 25, 2022 from IP address 155.198.10.231.

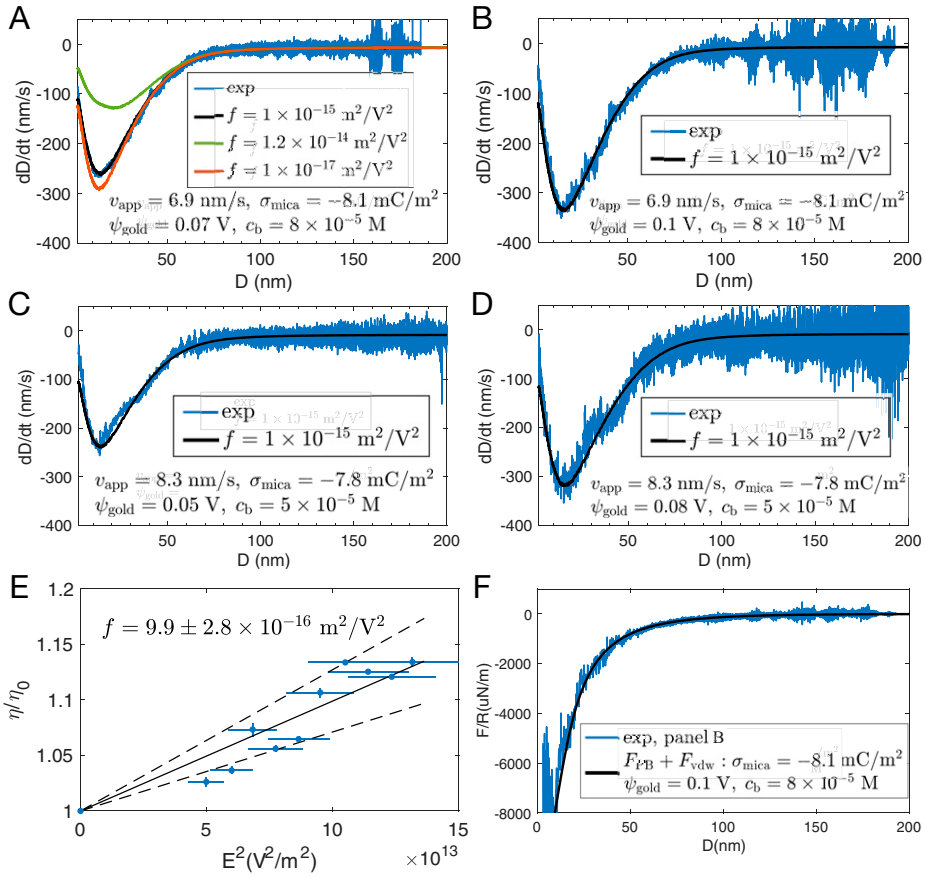

Fig. 4. (*A*)–(*D*) show representative d*D*/d*t*(*D*) profiles (additional profiles in *SI Appendix*, Section 2). The two pairs, *A*, *B* and *C*, *D*, were acquired, respectively, in two independent experiments at the same contact point for each experiment but at two different applied potentials onto the gold surface (see text). Each profile was obtained by averaging over three to four jump-in trajectories (see *Materials and Methods*). The black curves are the theoretical fits using the best *f* value determined directly from the plot in *E*, while for comparison, the predicted behavior corresponding to the extremal values $f = 10^{-17}$ and 1.2×10^{-14} (m/V)^2 estimated in the literature (*SI Appendix*) are shown by the green and orange curves. (*E*) A plot of η/η_0 versus E^2 (see Eq. **4** and text following equation) whose slope is *f* (Eq. **1**), showing the best-fit value to be $f = 9.9 \pm 2.8 \times 10^{-16}$ m^2/V^2. Error bars correspond to SE of mean (for η/η_0 axis) and to estimated uncertainties in the PB fit parameters (*SI Appendix*) for the E^2 axis. (*F*) Comparing the theoretical surface force $F_{tot} = F_{PB} + F_{vdW}$ with the force evaluated from the experimentally measured *D*(*t*), i.e., the right-hand side of Eq. **2**, now using the directly determined $f = 9.9 \times 10^{-16}$ m^2/V^2 (*E*); the close fit over the entire *D* range contrasts with the discrepancy at *D* <~40 nm in Fig. 3*B* where *f* was set to 0.

Magnitude of Viscoelectric Effect Determined from Surface Approach Dynamics. To analyze the effect of the viscoelectric effect on the dynamics of approach, we evaluated d*D*/d*t*(*D*), Eq. **3**—obtained by rearranging Eq. **2**—from the *D*(*t*) variation determined directly from the video recording of the approach:

$$\frac{dD}{dt} = (F_{tot}D + kD_0D - kD^2 + kv_{app}\,Dt)\,\frac{1}{6\pi R^2\eta(1+fE^2)}. \quad [3]$$

The damping term now manifests the viscoelectric effect in the enhanced value of $\eta = \eta_0(1 + f \cdot E^2)$. The advantage of using d*D*/d*t*(*D*) as the metric as opposed to *F*(*D*) is that, given that *D*(*t*) is the primary measurable through the FECO position (Fig. 3*B*), the error propagated from *D* is minimized by allowing only one linear operation on the parameter.

Fig. 4 shows several typical d*D*/d*t*(*D*) profiles, taken at different extracted values of the surface parameters, all showing these common features: at large separations, d*D*/d*t*(*D*) is equal to the driving speed v_{app} of the piezo crystal (<10 nm/s), while at smaller separations, *D* < ~80 nm, the approach velocity increases under the increasing electrostatic attraction while being modulated by the viscosity-dependent hydrodynamic stress as in Eq. **3**. At $D = D_{min}$ ~10 to 20 nm, a local minimum in d*D*/d*t*(*D*) is seen due to the decreasing driving term $F_{tot} \cdot D$ at small distances. Physically, this may be understood as follows: The electrostatic component of the attractive force F_{tot} (Eq. **2**) arises largely because of the expulsion of counterion pairs between the oppositely charged surfaces (38, 39), and its magnitude, for surface separations *D* of order the Debye screening length or less for our sphere-on-flat geometry, scales approximately as (1/*D*) (39). This is similar to the *D* variation of the damping term in Eq. **2**, so that the surfaces initially accelerate toward each other under the increasing attractive force. For *D* < ~30 nm in the conditions of our experiments, however, solution of the PB equation shows that the attraction varies more weakly than (1/*D*) (38), while the damping term continues to increase as (1/*D*), leading to the deceleration and eventual decrease in d*D*/d*t* (*SI Appendix*, section 5). The two pairs of figure panels, Fig. 4 *A* and *B* and *C* and *D* show d*D*/d*t*(*D*) profiles measured in two independent experiments but at the same contact point in each experiment (i.e., identical values of c_b and σ_{mica} for each pair of figures, different for each pair), with only the potential applied on the gold surface being varied. A higher applied potential on gold, from 0.07 V in Fig. 4*A* to 0.1 V in Fig. 4*B* and from 0.05 V in Fig. 4*C* to 0.08 V in Fig. 4D, results in higher jump-in speed at all distances as expected and ~70 nm/s and 85 nm/s differences, respectively,

Downloaded from https://www.pnas.org by Imperial College London Library on August 25, 2022 from IP address 155.198.10.231.

at the $dD/dt(D)$ local minima of Fig. 4 *B* and *D* compared with Fig. 4 *A* and *C*.

To evaluate the viscoelectric coefficient *f*, first we evaluated *D(t)* and $dD/dt(D)$ with $f = 0$ from Eq. **3** using the theoretically predicted F_{tot} with values of σ_{mica}, ψ_{gold}, and c_b extracted directly from the large *D* (>40 nm) force profile as described previously. We then derive

$$\frac{\eta}{\eta_0} = \frac{dD/dt_{f=0}}{dD/dt_{exp}} \cdot \frac{g_{exp}}{g_{f=0}}, \qquad [4]$$

where

$$g = \left(F_{tot}D + kD_0D - kD^2 + kv_{app}Dt\right),$$

which can be evaluated for the range of *E* values in the most relevant distances 8 nm < *D* < 30 nm. A plot of η/η_0 versus E^2 is shown in Fig. 4*E*, using values extracted from the dD/dt curves with least noise (Fig. 4 *A* and *B*) (for η/η_0) and from the PB equation (for E^2, Fig. 1*B*). Data were binned at equally spaced intervals of E^2 and averaged. From Eq. **1**, the slope of this plot is simply the viscoelectric coefficient *f*, and its best fit value is $f = 9.9 \pm 2.8 \times 10^{-16}$ m^2/V^2. To confirm this, $dD/dt(D)$ was solved with this value of *f* for each of the dD/dt curves in Fig. 4 *A*–*D*, showing excellent agreement [as also for additional $dD/dt(D)$ profiles in *SI Appendix*, Section 2]. In particular, this is seen comparing the fits of Eq. **3** to the data in Fig. 4 *A* and *B* and *C* and *D*, with each pair taken at the same contact point (in independent experiments) but at different ψ_{gold}; crucially, the best fits to the experimental $dD/dt(D)$ data are associated with the same *f* value for all four $dD/dt(D)$ profiles, even though the uniform fields across the gap at *D* < ~40 nm are significantly different. For comparison, the predicted curves according to Eq. **3** but using *f* values corresponding to the highest and lowest literature estimates to date (*SI Appendix*, Section 7) are also shown in Fig. 4*A*, showing clearly that they do not fit the data [similar misfits of these extremal *f* values to the data apply to the other $dD/dt(D)$ profiles but are omitted for clarity]. Finally, in Fig. 4*F*, we revisit the force profiles (*F*/*R*) versus *D*, Fig. 3, for which the discrepancy between theory and the forces evaluated from Eq. **2** for *D* < ~40 nm arose from ignoring the viscoelectric effect (i.e., setting $f = 0$ in Eq. **2**): We see that once the directly determined value of *f* is inserted into Eq. **2**, there is close agreement (within the scatter) between the evaluated forces and the theoretical prediction, further supporting our determination of the viscoelectric coefficient.

Conclusions

We have measured the viscoelectric effect in water by directly determining the changes in water viscosity under uniform electric fields through its modulation of the hydrodynamic damping between two approaching surfaces. Our result differs by up to one to two orders of magnitude from many of the earlier indirect estimates (7, 11, 12, 14–21), which were in the range $(10^{-14}$–$10^{-17})$ $(m/V)^2$ (*SI Appendix*, Section 7) (though some of these indirect estimates, e.g., Refs. 7 and 8, were comparable to our measured one). Molecular dynamics simulation results suggest lower *f* values at fields much higher than in our study (4, 5, 40) and also that the relation of Eq. **1** may not apply at such fields, while our results (Fig. 4*E*) are consistent with Eq. **1**. We do not know the reason for these discrepancies between experiment and MD simulations, though we should note that the fields used in the simulations could not be implemented over the length scales of water thickness in our experiments (10 to 30 nm), as electrolysis would occur (41); for this reason, comparison may not be appropriate. The main difference between our direct determination and previous estimates is that the latter were based on leveraging the electric field from the rapidly decaying potential gradient of double layers formed at a surface (or the field between two similar surfaces, which switches sign at the midplane due to symmetry). The analysis in those cases was based on an averaged electric field in the thin interfacial layer or in the intersurface gap (within which it varied very strongly), while in our study, the intersurface potential variation was very closely linear and its gradient—the electric field—therefore uniform across the water. We believe therefore that our measured value may be viewed as a direct measurement of the viscoelectric effect in water, conceptually similar to the direct measurements of this effect in polar organic liquids commenced over 80 y ago (1–3) but differing from all previous estimates of this effect in water, none of which involved measuring viscosity changes in uniform fields. It thus provides a benchmark of the viscoelectric effect, a basic phenomenon associated with coupling of the electric field to the dipole of water molecules, after decades of estimates covering a range of values differing by over a thousandfold. Improved characterization of the viscoelectric effect may shed light on many electrokinetic problems and help interpret boundary effects in aqueous environment, which has significant impact in real-life applications, as well as underpinning attempts at a better understanding of its molecular origins (4–6).

Materials and Methods

SFB. As illustrated in Fig. 2*A*, two plano-cylindrical glass lenses are arranged in a cross-cylinder configuration, with interaction geometry equivalent to a sphere approaching a flat surface. The upper lens is coated with a gold surface prepared through template stripping (30). The lower lens is covered by a single-crystal, back-silvered mica sheet. The upper lens is driven by the piezo crystal in a steady motion enabled by a function generator at a speed v_{app} < 10 nm/s toward the lower lens, mounted on a spring (constant $k = 89$ mN/mm), which bends in response to the total force between the surfaces. Normal force measurements were acquired from the bending of the spring *k* and by analyzing the hydrodynamics (Eq. **2**). The three-electrode configuration (Fig. 2*C*) enables positive potentials to be imposed onto the gold surface through a potentiostat when the platinum electrodes are positioned in the water immersing the surfaces, contained in a quartz bath to prevent short to ground. Further details of the technique are provided elsewhere (28, 32).

Preparation of Template-Stripped Gold Surface. The gold surfaces were prepared by evaporating 99.999% pure gold pellet (Kurt J. Lesker and Materion) with Fabmated crucible onto atomistically smooth mica leaflets prepared by cleaving. The gold surface was glued to a cylindrical fused-silica lens (curvature radius *R* ~1 cm) with epoxy resin (EPON Resin 1004F), and the mica leaflet was removed, leaving a gold surface of root mean-square roughness ~0.2 nm (*SI Appendix*, Section 6). Further details of the template-stripping method are given elsewhere (30).

Water Purification. Water was purified with the Barnstead GenPure Pro Water Purification System, using high-performance ultraviolet assembly to reduce total organic content (TOC) to ultralow levels. The resistivity of the purified water is 18.2 MΩ · cm at 25 °C with TOC < 1 ppb.

Image Acquisition and Analysis. A Hamamatsu Fusion C14440-20UP camera was set up to capture image sequence of FECO directly from the spectrometer without any lens in between. A calibration image was captured with a mercury (neon) calibration lamp, from which a linear relation between the pixel position and the wavelength was fitted. The image resolution is ~0.4 Å in wavelength per pixel, and the best achieved resolution in surface-to-surface separation per pixel is 2.3 Å with mica leaflets thinner than 3 μm. During the jump-in events, images were acquired at 993 fps. The pixel position of the fringe tip, corresponding to the minimal distance between the lenses, was evaluated by fitting a double Gaussian function to the pixel intensity of the fringe doublet (Fig. 2*B*). The separation *D* was evaluated using the multilayer matrix method, as described in previous works (30, 32, 42, 43).

Post–Data-Acquisition Processing. To reduce the noise in the separation *D*(*t*) trajectory, multiple recordings were acquired consecutively at the same contact point for each applied gold surface potential. *D*(*t*) was smoothed with a moving average filter at 0.02 s intervals, chosen carefully to avoid artifacts from smoothing. $dD(t)/dt$ was computed and averaged over repeated trajectories to reduce noise (*SI Appendix*, Section 3). Note that, as demonstrated

Downloaded from https://www.pnas.org by Imperial College London Library on August 25, 2022 from IP address 155.198.10.231.

previously, charge inversion on the gold surface alone neutralizes the mica surface charge when in contact. Therefore, hysteresis observed in consecutive jump-in events of mica–mica systems due to unequilibrated charge release (44) is not observed in the gold–mica system (28).

Fitting Parameters in PB Equation. The nonlinearized PB equation with constant potential on the gold surface and constant charge on the mica surface was solved numerically for more than 2,000 combinations of $\psi_{mica}(D = \infty)$, $\psi_{gold}(\forall D)$, and bulk concentration c_b, to sample $\psi_{mica}(D = \infty)$ at 0.01 V intervals, $\psi_{gold}(\forall D)$ at 0.01 V intervals, and bulk concentration c_b from 5×10^{-7} to 8×10^{-5} M at 1×10^{-6} M intervals. Each PB solution was augmented by van der Waals force $F_{vdW}(D) = A_H/6D^2$ with Hamaker constant $A_H = 9 \times 10^{-20}$ J (28, 32). The total force F_{tot} was compared to the normal force profile, i.e., the right-hand side of Eq. **2** ($\eta = \eta_0$), which was evaluated using the smoothed $D(t)$ as described previously, averaged over repeated profiles, and smoothed with a 0.05 s interval moving average filter. Best fit was selected using the least mean-square deviation at large separations ($D > 40$ nm) where the viscoelectric effect is small, subject only to the constraint $f \geq 0$. For each selected set of parameters, $\psi_{mica}(D)$ and $\sigma_{gold}(D)$ are evaluated for demonstrating charge inversion and for estimating the electric field $E(D)$ at varying separations (Fig. 1 *A* and *C*, and *SI Appendix*, section 1). Uncertainties in these parameters manifest as uncertainties in the evaluated electric field and are indicated as error bars in the data of Fig. 4*E*.

Numerical Solution to the Equation of Motion. Eq. **3** was made dimensionless by introducing

$$D = D^*L, \qquad v_{app} = v^*_{app}U, \qquad F_{tot} = F^*_{tot}F, \qquad k = k^*\frac{F}{L}, \qquad t = t^*\frac{L}{U},$$

which gives

$$\frac{dD^*}{dt^*} = N_0\left(F^*_{tot}D^* + k^*D^*_0D^* - k^*D^{*2} + k^*v^*_{app}D^*t^*\right)$$

$$N_0 = \frac{FL}{6\pi R^2\eta_0 U(1 + fE^2)}, \qquad [5]$$

where the dimensionless number N_0 indicates the relative scale of the surface forces compared to the viscous force. Eq. **5** was solved numerically using the second-order Crank-Nicolson method (45), taking $F_{tot}(D)$ and the corresponding $E(D)$ as inputs. v_{app} was evaluated by linear fits to the experimentally measured $D(t)$ at large separations $D > 200$ nm, where F_{tot} and spring force are mostly absent. Parameters used were spring constant $k = 89$ N/m, lens radius $R = 0.01$ m, bulk water viscosity at room temperature $\eta_0 = 8.9 \times 10^{-4}$ Pa · s, and initial separation $D_0 = 500$ nm. To avoid spurious computational errors due to the exponentially growing $|F_{tot}|$ as D decreases, the dimensionless time step Δt_n* at each discrete step n was adjusted as

$$\Delta t^*_n = \sqrt{L_{n-1}/U_{n-1} \cdot 10^{-5}s^{-1}},$$

and by updating the force scale F, the length scale L, and the velocity scale U such that

$$L_n = D^*_{n-1} \cdot L_{n-1}, \qquad U_n = \frac{|D^*_{n-1} - D^*_{n-2}| \cdot U_{n-1}}{\Delta t^*_{n-1}}, \qquad F_n = F_{tot}\left(D^*_{n-1}L_{n-1}\right),$$

where the initial values are $L_0 = D_0$, $U_0 = v_{app}$, and $F_0 = F_{tot}(D_0)$.

Data Availability. All study data are included in the article and/or supporting information.

ACKNOWLEDGMENTS. We thank Alexander Vaskevitch and Sam Safran for valuable comments, Gilad Silbert for providing the numerical solver to the PB equation, Yu Zhang and Ran Tivony for assistance with experiments, and George Degen for assisting us with the camera technique. We also thank the McCutchen Foundation, the Israel Science Foundation-National Natural Science Foundation of China joint program (ISF-NSFC Grant 2577/17), and the Israel Science Foundation (Grant ISF 1229/20) for their support of this work. This project has received funding from the European Research Council under the European Union's Horizon 2020 research and innovation programme (Grant Agreement 743016). This work was made possible in part by the historic generosity of the Harold Perlman family.

1. E. N. D. C. Andrade, C. Dodd, Effect of an electric field on the viscosity of liquids. *Nature* **144**, 117–118 (1939).
2. E. N. D. C. Andrade, C. Dodd, The effect of an electric field on the viscosity of liquids. *Proc. R. Soc. Med.* **187**, 296–337 (1946).
3. E. N. D. C. Andrade, C. Dodd, The effect of an electric field on the viscosity of liquids. II. *Proc. R. Soc. Lond. A Math. Phys. Sci.* **204**, 449–464 (1951).
4. M. Shafiei, M. von Domaros, D. Bratko, A. Luzar, Anisotropic structure and dynamics of water under static electric fields. *J. Chem. Phys.* **150**, 074505 (2019).
5. D. Zong, H. Hu, Y. Duan, Y. Sun, Viscosity of water under electric field: Anisotropy induced by redistribution of hydrogen bonds. *J. Phys. Chem. B* **120**, 4818–4827 (2016).
6. J. M. Kahk, B. H. Tan, C. D. Ohl, N. D. Loh, Viscous field-aligned water exhibits cubic-ice-like structural motifs *Phys. Chem. Chem. Phys.* **20**, 19877–19884 (2018).
7. R. J. Hunter, J. V. Leyendekk, Viscoelectric coefficient for water. *J. Chem. Soc., Faraday Trans. I* **74**, 450–455 (1978).
8. J. Lyklema, J. T. G. Overbeek, On the interpretation of electronic potentials. *J. Colloid Sci.* **16**, 501–512 (1961).
9. P. J. Scales, F. Griezer, T. H. Healy, Electrokinetics of the muscovite mica-aqueous solution interface. *Langmuir* **6**, 582–589 (1990).
10. L. Ma, A. Gaisinskaya-Kipnis, N. Kampf, J. Klein, Origins of hydration lubrication. *Nat. Commun.* **6**, 6060 (2015).
11. W.-L. Hsu *et al.*, Viscoelectric effects in nanochannel electrokinetics. *J. Phys. Chem. C* **121**, 20517–20523 (2017).
12. T. Sen, M. Barisik, Slip effects on ionic current of viscoelectric electroviscous flows through different length nanofluidic channels. *Langmuir* **36**, 9191–9203 (2020).
13. P. Neogi, E. Ruckenstein, Viscoelectric effects in reverse osmosis. *J. Colloid Interface Sci.* **79**, 159–169 (1981).
14. B. J. Carroll, Electrokinetic and Surface Potentials, PhD thesis, Cambridge University, Cambridge, UK, (1970).
15. D. A. Haydon, in *Recent Progress in Surface Science*, J. F. Danielli, K. G. A. Pankhurst, A. C. Riddiford, Eds. (Academic Press, London, 1964), p. 140.
16. W.-L. Hsu, H. Daiguji, D. E. Dunstan, M. R. Davidson, D. J. E. Harvie, Electrokinetics of the silica and aqueous electrolyte solution interface: Viscoelectric effects. *Adv. Colloid Interface Sci.* **234**, 108–131 (2016).
17. R. J. Hunter, The interpretation of electrokinetic potentials. *J. Colloid Interface Sci.* **22**, 231–239 (1966).
18. D. Stigter, On the viscoelectric effect in colloidal solutions. *J. Phys. Chem.* **68**, 3600–3602 (1964).
19. J. T. Webb, P. D. Bhatnagar, D. G. Williams, The interpretation of electrokinetic potentials and the inaccuracy of the DLVO theory for anatase sols. *J. Colloid Interface Sci.* **49**, 346–361 (1974).
20. F. Liu, A. Klaassen, C. Zhao, F. Mugele, D. Van Den Ende, Electroviscous dissipation in aqueous electrolyte films with overlapping electric double layers. *J. Phys. Chem. B* **122**, 933–946 (2018).
21. S. Olejnik, J. W. White, Thin layers of water in vermiculites and montmorillonites – Modification of water diffusion. *Nat. Phys. Sci (Lond.)* **236**, 15–16 (1972).
22. S. O. Diallo, E. Mamontov, W. Nobuo, S. Inagaki, Y. Fukushima, Enhanced translational diffusion of confined water under electric field. *Phys. Rev. E. Stat. Nonlin. Soft Matter Phys.* **86**, 021506 (2012).
23. M. Carmo, D. L. Fritz, J. Mergel, D. Stolten, A comprehensive review on PEM water electrolysis. *Int. J. Hydrogen Energy* **38**, 4901–4934 (2013).
24. M. Szklarczyk, R. C. Kainthla, J. O. M. Bockris, On the dielectric breakdown of water: An electrochemical approach. *J. Electrochem. Soc.* **136**, 2512–2521 (1989).
25. J. N. Israelachvili, *Intermolecular and Surface Forces* (Academic Press, Waltham, ed. 3, 2011).
26. R. M. Pashley, Hydration Forces between Mica Surfaces in Aqueous Electrolyte Solutions. *J. Colloid Interface Sci.* **80**, 153–162 (1981).
27. S. A. Safran, *Statistical Thermodynamics of Surfaces, Interfaces and Membranes* (Addison-Wesley, New York, 1994).
28. R. Tivony, N. Iuster, J. Klein, Probing the surface properties of gold at low electrolyte concentration. *Langmuir* **32**, 7346–7355 (2016).
29. J. Klein, E. Kumacheva, Simple liquids confined to molecularly thin layers. I. Confinement-induced liquid to solid phase transitions. *J. Chem. Phys.* **108**, 6996–7009 (1998).
30. L. Chai, J. Klein, Large area, molecularly smooth (0.2 nm rms) gold films for surface forces and other studies. *Langmuir* **23**, 7777–7783 (2007).
31. L. Chai, "Forces between polymers and charge-bearing surfaces across aqueous media," PhD thesis, Weizmann Institute of Science, Rehovot, Israel (2007).
32. R. Tivony, D. B. Yaakov, G. Silbert, J. Klein, Direct observation of confinement-induced charge inversion at a metal surface. *Langmuir* **31**, 12845–12849 (2015).
33. N. Kampf, D. Ben-Yaakov, D. Andelman, S. A. Safran, J. Klein, Direct measurement of sub-Debye-length attraction between oppositely charged surfaces. *Phys. Rev. Lett.* **103**, 118304 (2009).
34. F. Booth, N. F. Mott, The electroviscous effect for suspensions of solid spherical particles. *Proc. R. Soc. Lond. A Math. Phys. Sci.* **203**, 533–551 (1950).
35. M. Banik, P. Ghosh, The electroviscous effect at fluid–fluid interfaces. *Ind. Eng. Chem. Res.* **52**, 1581–1590 (2013).
36. A. Behjatian, M. Bespalova, N. Karedla, M. Krishnan, Electroviscous effect for a confined nanosphere in solution. *Phys. Rev. E* **102**, 042607 (2020).
37. J. N. Israelachvili, Measurement of the viscosity of liquids in very thin films. *J. Colloid Interface Sci.* **110**, 263–271 (1986).

Downloaded from https://www.pnas.org by Imperial College London Library on August 25, 2022 from IP address 155.198.10.231.

38. A. A. Meier-Koll, C. C. Fleck, H. H. von Grunberg, The counterion-release interaction. *J. Phys. Condens. Matter* **16**, 6041–6052 (2004).
39. S. A. Safran, Scaling relations for counterion release and attraction of oppositely charged surfaces. *Europhys. Lett.* **69**, 826–831 (2005).
40. A. Baer, Z. Miličević, D. M. Smith, A.-S. Smith, Water in an electric field does not dance alone: The relation between equilibrium structure, time dependent viscosity and molecular motions. *J. Mol. Liq.* **282**, 303–315 (2019).
41. H. Ohta *et al.*, Field-induced water electrolysis switches an oxide semiconductor from an insulator to a metal. *Nat. Commun.* **1**, 118 (2010).
42. M. Born, E. Wolf, *Principles of Optics: Electromagnetic Theory of Propagation, Interference and Diffraction of Light* (Cambridge University Press, Cambridge, ed. 7, 1999).
43. M. T. Clarkson, Multiple-beam interferometry with thin metal films and unsymmetrical systems. *J. Phys. D Appl. Phys.* **22**, 475–482 (1989).
44. U. Raviv, P. Laurat, J. Klein, Time dependence of forces between mica surfaces in water and its relation to the release of surface ions. *J. Chem. Phys.* **116**, 5167–5172 (2002).
45. J. Crank, P. Nicolson, A practical method for numerical evaluation of solutions of partial differential equations of the heat-conduction type. *Math. Proc. Camb. Philos. Soc.* **43**, 50–67 (1947).

Downloaded from https://www.pnas.org by Imperial College London Library on August 25, 2022 from IP address 155.198.10.231.